Two-Dimensional Materials for Infrared Detection

George Zhang

Electrical Engineering and Computer Sciences
University of California, Berkeley

Technical Report No. UCB/EECS-2021-12
http://www2.eecs.berkeley.edu/Pubs/TechRpts/2021/EECS-2021-12.html

May 1, 2021

Copyright © 2021, by the author(s).
All rights reserved.

Permission to make digital or hard copies of all or part of this work for personal or classroom use is granted without fee provided that copies are not made or distributed for profit or commercial advantage and that copies bear this notice and the full citation on the first page. To copy otherwise, to republish, to post on servers or to redistribute to lists, requires prior specific permission.

Acknowledgement

First, I would like to thank my advisor, Professor Ali Javey, for the rare opportunity to research among his prolific team and for his strong support and guidance throughout my graduate career. Second, I would like to thank Dr. Matin Amani, Dr. Chaoliang Tan, and Professor James Bullock for their constant mentorship. Third, I would like to thank Professor Vivek Subramanian, Professor Eli Yablonovitch, and Professor Ana Arias for sharing their research passions through excellent teaching. Finally, I would like to thank my family for all of the sacrifices they have made for me.

Two-Dimensional Materials for Infrared Detection

by George Zhang

Research Project

Submitted to the Department of Electrical Engineering and Computer Sciences, University of California at Berkeley, in partial satisfaction of the requirements for the degree of **Master of Science, Plan II**.

Approval for the Report and Comprehensive Examination:

Committee:

Professor Ali Javey
Research Advisor

5/9/2019
(Date)

* * * * * * *

Professor Ana Arias
Second Reader

5/13/2019
(Date)

Scanned by CamScanner

Acknowledgements

First, I would like to thank my advisor, Professor Ali Javey, for the rare opportunity to research among his prolific team and for his strong support and guidance throughout my graduate career. Second, I would like to thank Dr. Matin Amani, Dr. Chaoliang Tan, and Professor James Bullock for their constant mentorship. Third, I would like to thank Professor Vivek Subramanian, Professor Eli Yablonovitch, and Professor Ana Arias for sharing their research passions through excellent teaching. Finally, I would like to thank my family for all of the sacrifices they have made for me.

Abstract

All matter above absolute zero temperature, including our bodies and planets light years away, emits thermal infrared radiation. Thus, infrared detection plays a large role in the modern world, as can be seen in thermal imaging, wireless control, and observational astronomy. The infrared wavelength range may be divided into near-infrared (NIR, 0.7–1 μm), short-wave infrared (SWIR, 1–3 μm), mid-wave infrared (MWIR, 3–5 μm), long-wave infrared (LWIR, 7–14 μm), and very-long-wave infrared (VLWIR, 12–30 μm) regions. Human body thermal radiation is centered around 9.5 μm, thus LWIR is of high interest for applications such as night-vision detection of humans. Researchers are currently searching through the class of two-dimensional (2D) materials for a LWIR-absorbing material. 2D materials, which have demonstrated excellent electrical and optical properties, offer a low-profile, potentially high-performance solution for night-vision detection. Platinum diselenide ($PtSe_2$) is currently the only 2D material experimentally reported in literature to absorb up to LWIR. However, the responsivity of $PtSe_2$ photoconductors suffers greatly at LWIR wavelengths.

This technical report presents electrical and optical characterization of three 2D materials: palladium diselenide ($PdSe_2$), tellurium (Te), and platinum/sulfur/selenium ($PtS_{2-x}Se_x$) alloys. Just recently, researchers have claimed $PdSe_2$ to be a LWIR material, however we show through rigorous optical and electrical characterization that $PdSe_2$ is instead a SWIR material. Solution-synthesized Te is introduced as a high-performance SWIR material. Lastly, we show progress on $PtS_{2-x}Se_x$ alloys, which surpasses $PtSe_2$ in terms of responsivity at LWIR wavelengths.

Contents

Contents i

List of Figures ii

1 Introduction 1

1.1 Two-Dimensional Materials for Long-Wave Infrared Detection 1

1.2 2D Noble-Metal Dichalcogenides 2

1.3 2D $PdSe_2$ for SWIR Detectors 2

1.4 2D Te for High-Performance SWIR Detectors 3

1.5 2D $PtS_{2-x}Se_x$ Alloys for LWIR Detectors 3

2 Experimental Results 4

2.1 2D $PdSe_2$ Characterization 4

2.2 2D Te Characterization 13

2.3 2D $PtS_{2-x}Se_x$ Characterization 14

3 Conclusion 16

3.1 2D $PdSe_2$ 16

3.2 2D Te 16

3.3 2D $PtS_{2-x}Se_x$ 17

Bibliography 18

List of Figures

2.1 Materials characterization of $PdSe_2$… 4

2.2 Optical characterization of $PdSe_2$… 5

2.3 Optical characterization of bulk $PdSe_2$… 6

2.4 Optical microscope images of the $PdSe_2$ flakes… 8

2.5 Bandgap extraction of $PdSe_2$… 9

2.6 Transmission and reflection spectra of a 134 nm thick $PdSe_2$ flake… 9

2.7 Electrical characterization of $PdSe_2$… 10

2.8 Photoresponse of $PdSe_2$ photoconductors… 12

2.9 2D Te characterization… 13

2.10 2D $PtS_{2-x}Se_x$ characterization… 14

Chapter 1

Introduction

1.1 Two-Dimensional Materials for Long-Wave Infrared Detection

Since the discovery of ultrathin graphite [1] and molybdenum disulfide (MoS_2) [2], [3] and the demonstration of two-dimensional (2D) electronic transport in graphene [4], [5], researchers have explored the properties and applications of 2D materials in great depth. 2D materials have exhibited exceptional performance in optics and electronics with photoluminescence quantum yields approaching unity [6], [7] and ultrafine scaling of field-effect transistors (FETs) [8], [9]. Thus, given the interest in long-wave (8–14 μm) infrared (LWIR) detection to capture human body thermal radiation (λ_{peak} ~ 9.5 μm) [10] for night vision, 2D materials are natural candidates.

2D materials such as black phosphorus (bP) [11], [12] and tellurium (Te) [13] have been utilized for high-performance short-wave (1–2.7 μm) infrared (SWIR) to mid-wave (3–5 μm) infrared (MWIR) photodetectors. Platinum diselenide ($PtSe_2$) is the only 2D material experimentally reported in literature to absorb LWIR, but with very low responsivity at LWIR wavelengths [14].

Just recently, palladium diselenide ($PdSe_2$) has been reported to have metallic bulk characteristics [15] and LWIR detection beyond 15 μm [16]. However, these claims are unfounded due to errors in analysis, to be discussed further. We have performed a rigorous study on the optical and electrical properties of $PdSe_2$, showing instead that $PdSe_2$ is a SWIR material [17]. Nonetheless, there exist 2D materials that can absorb LWIR more efficiently than $PtSe_2$ can, as we have shown for the first time using platinum/sulfur/selenium $PtS_{2-x}Se_x$ alloys, to be discussed further.

1.2 2D Noble-Metal Dichalcogenides

Two-dimensional (2D) transition metal dichalcogenides (TMDCs) have attracted considerable attention and have been explored for numerous applications including electronics, optoelectronics, catalysis, and sensors in the last decade [18]. Motivated by the attractive properties and wide applications of TMDCs, researchers have explored other novel 2D two-element systems in hopes of unlocking new material properties and applications. Among these systems is the 2D noble-metal dichalcogenides (NMDCs) with the general formula MX_2 (where M=Pt, Pd and X=S, Se, Te) [19]. NMDCs have recently been synthesized and demonstrated to exhibit air stability and strongly thickness-dependent bandgaps. For example, $PtSe_2$ and PdS_2 exhibit a sharp thickness-modulated semiconductor-to-metal transition [20], [21], [22], whereas PtS_2 also shows strong thickness dependence but is a narrow-bandgap indirect semiconductor in bulk [23]. $PtTe_2$ and $PdTe_2$ are both semimetals [24], [25], with the latter exhibiting superconductivity [26], [27].

1.3 2D $PdSe_2$ for SWIR Detectors

$PdSe_2$, a NMDC, has also been synthesized and explored in the last few years. Field-effect transistors based on $PdSe_2$ flakes show electron mobilities up to ~200 $cm^2 V^{-1} s^{-1}$ [28]. $PdSe_2$ was experimentally reported to have a thickness-dependent bandgap, in which monolayer $PdSe_2$ has a bandgap of ~1.4 eV and bulk $PdSe_2$ is metallic with a bandgap approaching 0 eV [15]. More recently, $PdSe_2$ has been investigated for LWIR detectors [16]. In our work, we systematically study the optical and electrical properties of $PdSe_2$ with an emphasis on its thickness-dependent bandgap to determine future applications for this material. Our results show that $PdSe_2$ is an indirect semiconductor with a monolayer bandgap of 1.37 eV and a bulk bandgap of 0.5 eV (in contrast to previous works which have predicted metallic bulk), as shown by optical absorption and photoresponse measurements. Furthermore, the temperature-dependent electrical measurements of a 6.8-nm-thick $PdSe_2$ flake-based transistor shows effective electron mobilities of 130 and 520 $cm^2 V^{-1} s^{-1}$ at 300 K and 77 K, respectively. Owing to its relatively small bandgap, thick PdSe2 can be utilized for short-wave infrared (SWIR) photodetectors. A room-temperature

peak specific detectivity (D^*) of 6.4×10^{10} cm $Hz^{1/2}$ W^{-1} at 0.7 μm with a band edge at 1.94 μm is achieved on a 6.8-nm-thick $PdSe_2$ flake-based photodetector.

1.4 2D Te for High-Performance SWIR Detectors

Air-stable 2D Te has recently been grown via solution, exhibiting on/off ratios and field-effect mobilities as high as 10^6 and 700 cm^2 V^{-1} s^{-1}, respectively [29]. Since bulk Te is reported to have a bandgap of 0.35 eV, solution-synthesized 2D Te is a promising material for SWIR photodetectors. We have performed comprehensive optical and electrical characterization on 2D Te. We show that a 12-nm-thick Te flake-based transistor shows effective hole mobilities of 450 and 1430 cm^2 V^{-1} s^{-1} at 300 K and 77 K, respectively [13]. Through optical cavity engineering, we may also tune the peak responsivity of Te photoconductors from 1.4 μm to 2.4 μm with a cutoff wavelength of 3.4 μm, encompassing the full SWIR band [13].

1.5 2D $PtS_{2-x}Se_x$ Alloys for LWIR Detectors

As mentioned previously, $PtSe_2$ is the only 2D material experimentally reported to absorb LWIR [14] and is metallic in bulk, however its close relative, PtS_2, is an indirect narrow-bandgap semiconductor in bulk [23]. The elemental difference between these two materials is the sulfur (S) and selenium (Se) concentration. This raises the possibility that platinum/sulfur/selenium $PtS_{2-x}Se_x$ alloys may offer a very narrow but not metallic bulk bandgap. This is indeed the case, and these alloys have been incorporated into LWIR detectors with greater responsivities compared to those using pure $PtSe_2$. Our $PtS_{2-x}Se_x$ photodetectors can comfortably detect up to 11 μm even without pushing the Se concentration above 71%.

Chapter 2

Experimental Results

2.1 2D $PdSe_2$ Characterization

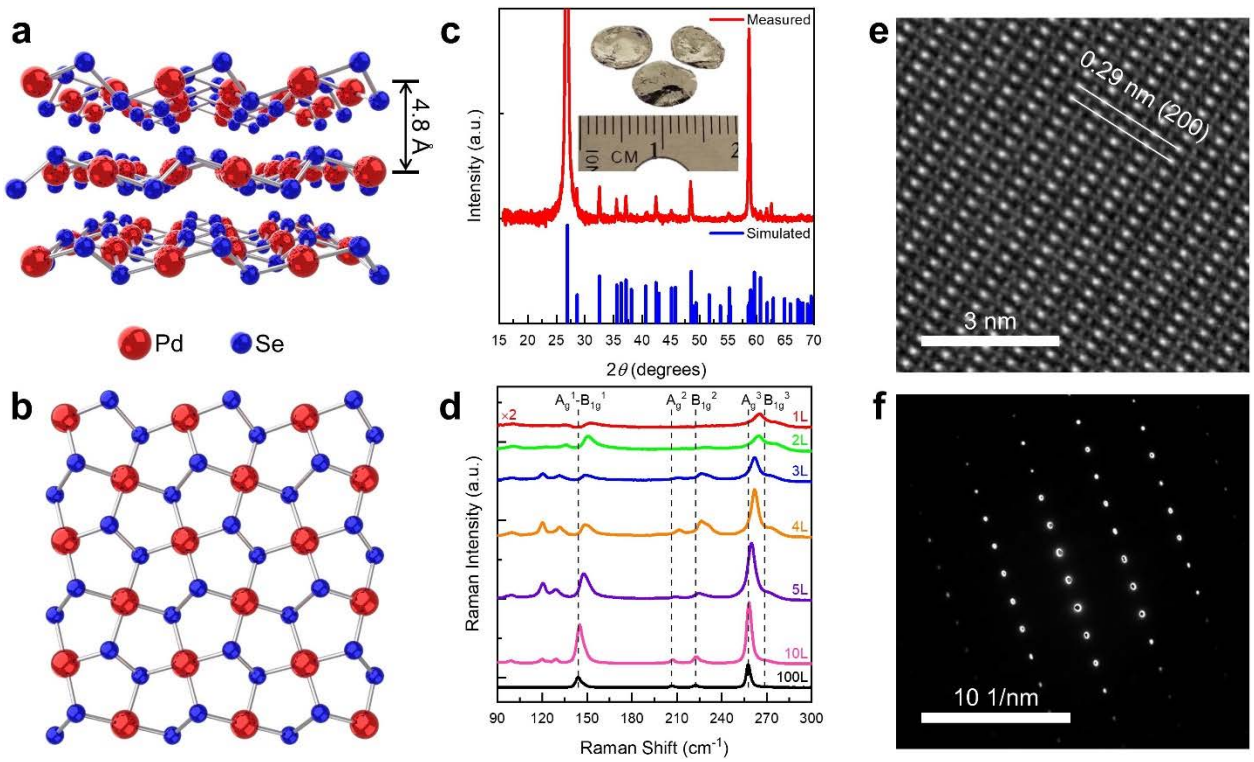

Figure 2.1: Material characterization of $PdSe_2$: Crystal structure of $PdSe_2$: (a) lateral and (b) top-down view. (c) Measured and simulated XRD spectra of a bulk PdSe2 crystal. (c) Raman spectra of PdSe2 for various thicknesses. (e) HR-TEM image and (f) SAED pattern of a 6.8-nm-thick PdSe2 flake.

The crystal structure of PdSe2 is shown in Figures 2.1(a)–2.1(b). $PdSe_2$ is a layered 2D material with a theoretical monolayer thickness of ~4.8 Å. $PdSe_2$ is also the first experimentally realized 2D material with pentagonal-structured layers [28], [15], as shown in Figure 2.1(b). Pentagonal 2D materials have been theoretically proposed [30], [31], though $PdSe_2$ is the first among these to

be synthesized and experimentally characterized as a 2D material. Figure 2.1(c) shows the measured X-ray diffraction (XRD) pattern of a bulk $PdSe_2$ crystal grown by chemical vapor transport (CVT), which is consistent with the simulated XRD pattern, confirming the synthesis of bulk single crystal $PdSe_2$. 2D $PdSe_2$ nanoflakes of varying thickness were mechanically exfoliated from a large single-crystalline source. Figure 2.1(d) shows the Raman spectra of $PdSe_2$ flakes of thicknesses ranging from monolayer to bulk. The locations of the Raman modes A_g^1-B_{g1}^1, A_g^2, B_{g1}^2, A_g^3, and B_{g1}^3 and their shifts with changing thickness are consistent with previous reports on $PdSe_2$ [15]. Figure 2.1(e) shows the high-resolution transmission electron microscope (HR-TEM) image of a 6.8-nm-thick $PdSe_2$ flake. The lattice constant is 0.29 nm, which can be assigned to the (200) planes of the $PdSe_2$ single crystal. The corresponding selected area electron diffraction (SAED) pattern shows a single set of bright diffraction dots (Figure 2.1(f)), further confirming the single crystalline nature.

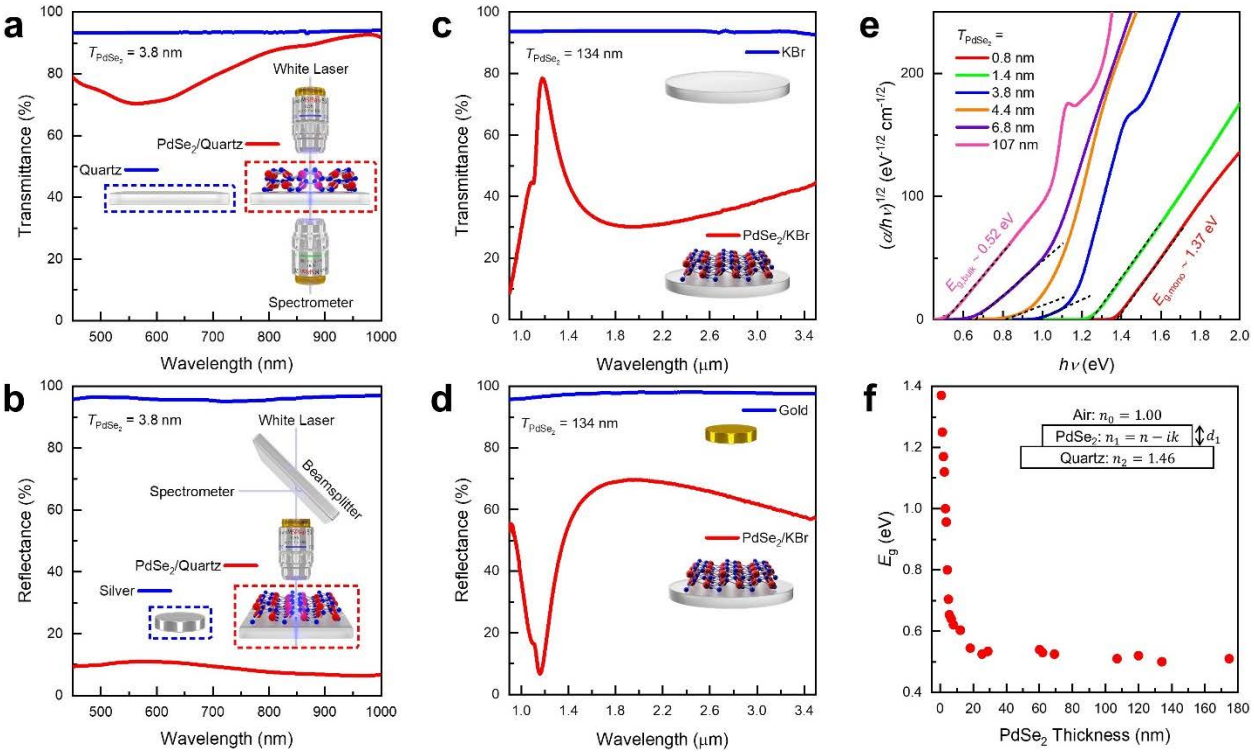

Figure 2.2: Optical characterization of $PdSe_2$: (a) Transmission and (b) reflection measurements of a 3.8-nm-thick $PdSe_2$ flake on a quartz substrate in the visible-wavelength range. (c) Transmission and (d) reflection measurements of a 134-nm-thick $PdSe_2$ flake on a KBr substrate in the infrared-wavelength range. (e) Optical indirect bandgap extraction of $PdSe_2$ for various thicknesses. (f) Optical indirect bandgap of $PdSe_2$ as a function of its thickness.

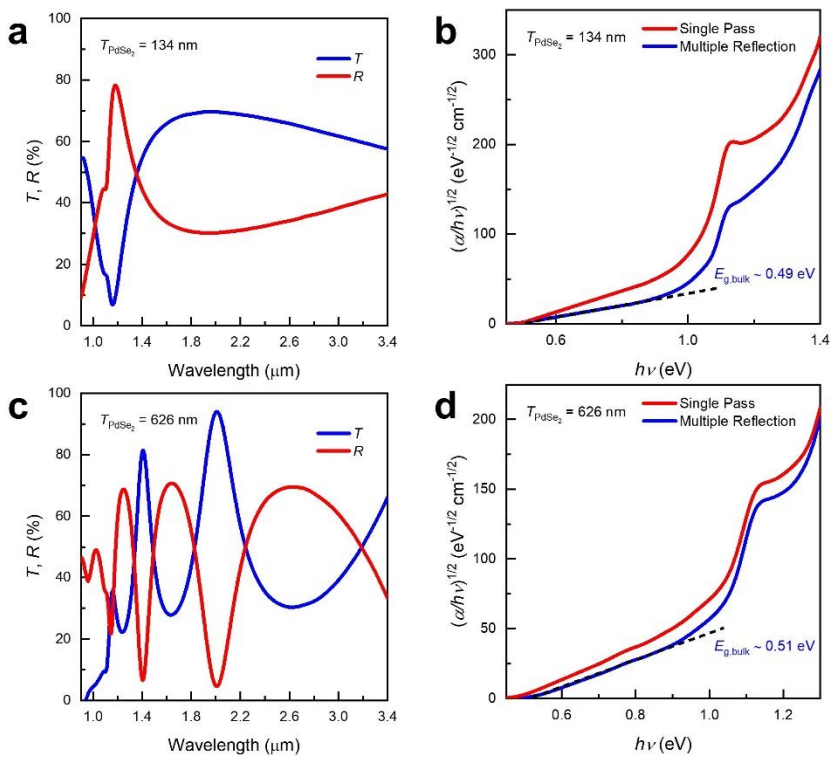

Figure 2.3: Optical characterization of bulk $PdSe_2$: (a) Transmission and reflection spectra of a 134-nm-thick $PdSe_2$ flake and its corresponding (b) optical indirect bandgap extraction. (c) Transmission and reflection spectra of a 626-nm-thick $PdSe_2$ flake and its corresponding (d) optical indirect bandgap extraction. Note that the reflection and transmission spectra of thicker $PdSe_2$ flakes show out-of-phase oscillations due to thin film interference, which are canceled out when calculating the absorption coefficient. For a single-pass calculation, the absorption coefficient $\alpha = (1/d)\log[(1-R)/T]$, where d is the thickness, and R and T are the reflectance and transmittance of the $PdSe_2$ flake. To account for multiple reflections in the $PdSe_2$ flake, $\alpha = 4\pi k/\lambda$, as discussed below.

To perform optical measurements, $PdSe_2$ flakes were exfoliated onto quartz by mechanical exfoliation and gold-mediated exfoliation [32], which can yield large-area mono- and few-layer $PdSe_2$ flakes. Optical transmittance and reflectance measurements were conducted in both a UV-Vis micro-absorption setup as well as a Fourier-transform infrared microscope. The combination of these techniques permits measurements over a wavelength range of 450 nm to 15 μm [6]. UV-Vis measurements were performed with reference to a blank quartz substrate and a silver mirror (Figure 2.2(a)–2.2(b)), while FTIR measurements were performed with reference to a blank quartz or KBr substrate and a gold mirror (Figure 2.2(c)–2.2(d)). Quartz is optically transparent for visible to SWIR wavelengths, whereas the transparency of KBr extends further a few micron beyond

LWIR wavelengths. Note that the reflectance and transmittance of thick $PdSe_2$ flakes show out-of-phase oscillations due to multiple reflections occurring in the 2D film; this destructive and constructive interference behavior is accounted for when calculating the absorption coefficient, as shown more clearly in Figure 2.3. We did not observe differences in transmittance and reflectance for PdSe2 flakes prepared by mechanical exfoliation and gold-mediated exfoliation. To account for thin-film interference in the PdSe2 flake, we used the transfer matrix method. For transmission and reflection of light by a thin film on a substrate, we define the Fresnel coefficients [33]:

$$r_1 = \frac{n_0 - n_1}{n_0 + n_1}, \quad t_1 = \frac{2n_0}{n_0 + n_1}, \\ r_2 = \frac{n_1 - n_2}{n_1 + n_2}, \quad t_2 = \frac{2n_1}{n_1 + n_2} \tag{1}$$

where $n_0 = 1.00$, $n_1 = n - ik$, and $n_2 = 1.46$ are the refractive indices of air, the $PdSe_2$ flake, and quartz, respectively. The reflected and transmitted amplitudes are:

$$R = \frac{r_1 + r_2 e^{-2i\delta_1}}{1 + r_1 r_2 e^{-2i\delta_1}}, \quad T = \frac{t_1 t_2 e^{-i\delta_1}}{1 + r_1 r_2 e^{-2i\delta_1}} \tag{2}$$

where $\delta_1 = (2\pi/\lambda)n_1 d_1$ and d_1 is the thickness of the $PdSe_2$ flake [33]. The reflectance and transmittance as ratios of the energy reflected and transmitted to the energy incident are [33]:

$$\boldsymbol{R}_{\text{sim}} = RR^*, \quad \boldsymbol{T}_{\text{sim}} = \frac{n_2}{n_0} TT^* \tag{3}$$

We then used the Nelder-Mead algorithm to minimize $(R\text{meas} - R\text{sim})^2 + (T\text{meas} - T\text{sim})^2$ to estimate the complex refractive index, $n_1 = n - ik$, of the $PdSe_2$ flake [34], [35]. Finally, we extracted the optical bandgap of the $PdSe_2$ flake from a Cody plot of $(\alpha/h\nu)^{1/2}$ versus $h\nu$, where $\alpha = 4\pi k/\lambda$ is the absorption coefficient of the $PdSe_2$ flake [34], as shown in Figure 2.2(e) for $PdSe_2$ flakes of varying thickness. The optical microscope images of these flakes along with their

thicknesses measured via atomic force microscopy (AFM) are shown in Figure 2.4. Figure 2.2(f) shows the measured optical indirect bandgap of $PdSe_2$ as a function of its thickness, which agrees with theoretical calculations in terms of the monolayer bandgap, but deviates from previously reported experimental data in terms of the bulk bandgap [15]. This experimental deviation is likely due to both accounting for thickness-dependent reflectance (in addition to thickness-dependent transmittance) as well as the broader spectral range (~0.35–3.1 eV) measured in this work, which fully encompasses the bandgap range of $PdSe_2$. A previous work on $PdSe_2$ extrapolated optical bandgap values from a measured spectral range of ~1.3–3.25 eV, which is nearly a whole eV beyond the bulk bandgap of $PdSe_2$ [15]. Accounting for thin-film interference only changes the bandgap by ~0.1 eV (supplementary material Figure S1) [15], whereas neglecting reflectance and extrapolating far beyond the bandgap can drastically alter the bandgap value (Figure 2.5). This can be clearly seen for reflection and transmission measurements performed on a 134-nm-thick $PdSe_2$ flake which shows an absorption edge around 2 μm (Figure 2.6).

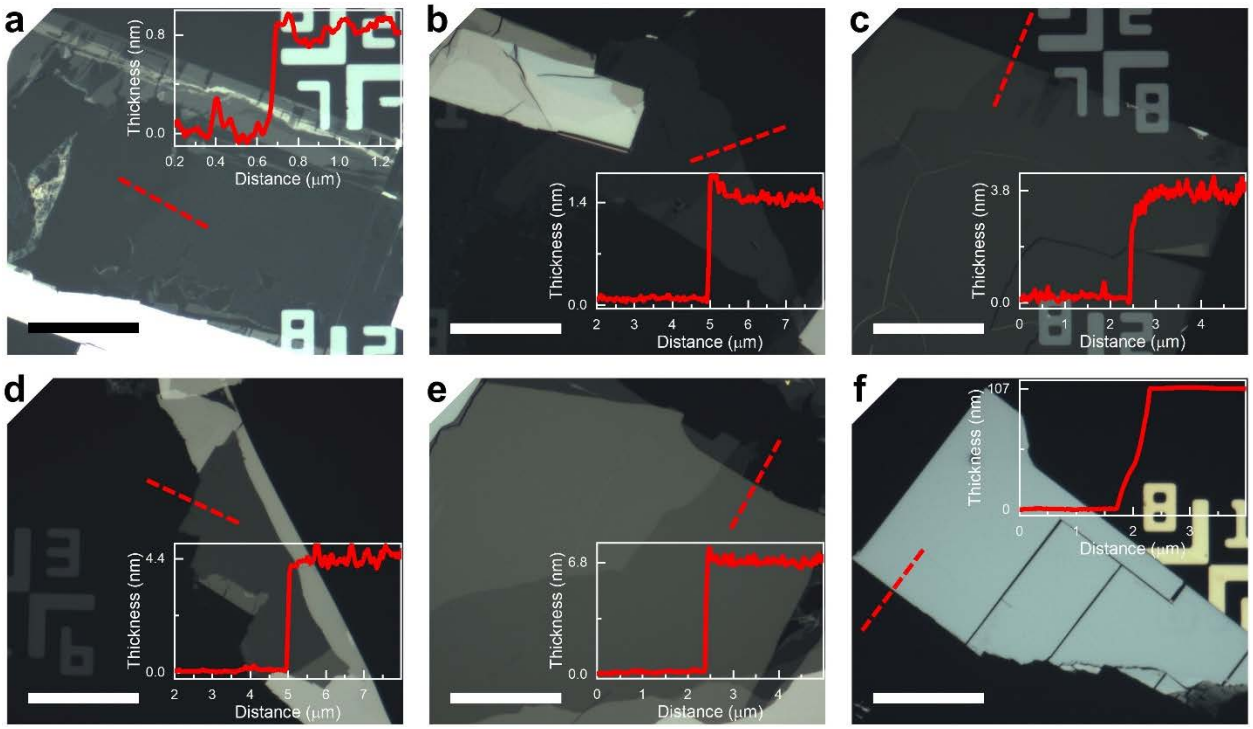

Figure 2.4: Optical microscope images of the $PdSe_2$ flakes used for reflection and transmission measurements in Figure 2(e) inset with atomic force microscopy (AFM) thickness measurements.

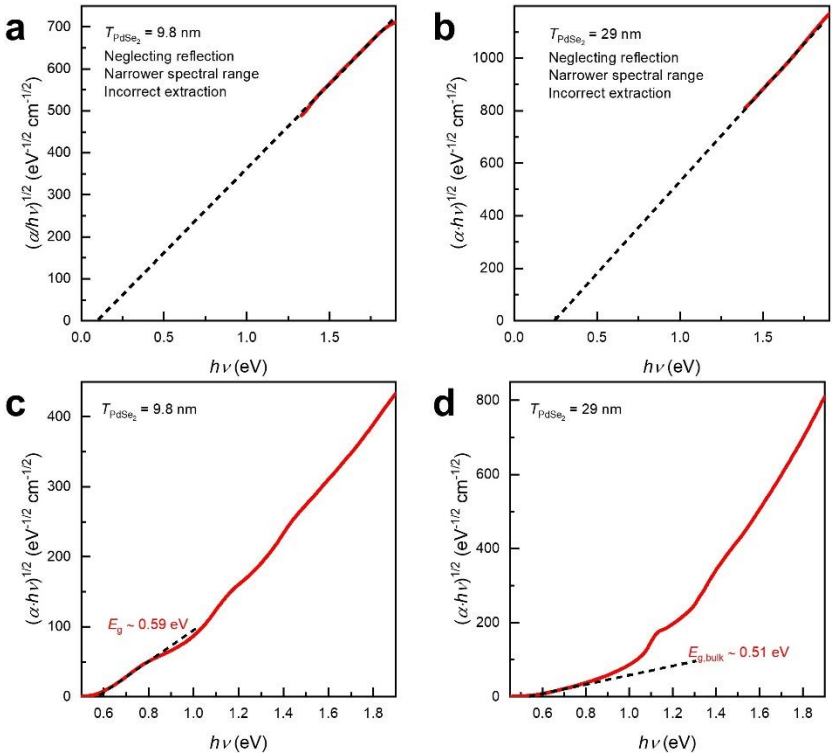

Figure 2.5: Bandgap extraction of $PdSe_2$: (a), (b) Cody and Tauc plots for 9.8 and 29 nm $PdSe_2$ flakes neglecting reflection and using a narrower spectral range, which results in incorrect and heavily underestimated bandgap extraction. (c), (d) Cody and Tauc plots for the same flakes using a broader spectral range and accounting for transmission, reflection, and thin-film interference, which results in more accurate bandgap extraction.

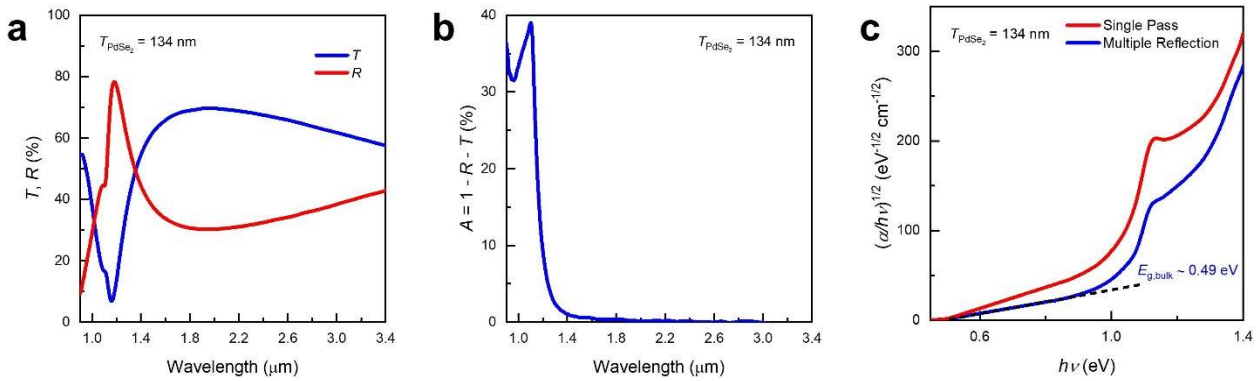

Figure 2.6: (a) Transmission and reflection spectra of a 134 nm thick $PdSe_2$ flake and its corresponding (b) absorption spectra and (c) optical indirect bandgap extraction. Note that the absorption edge is around 2 μm, but we may more accurately extract the bandgap from a Cody plot.

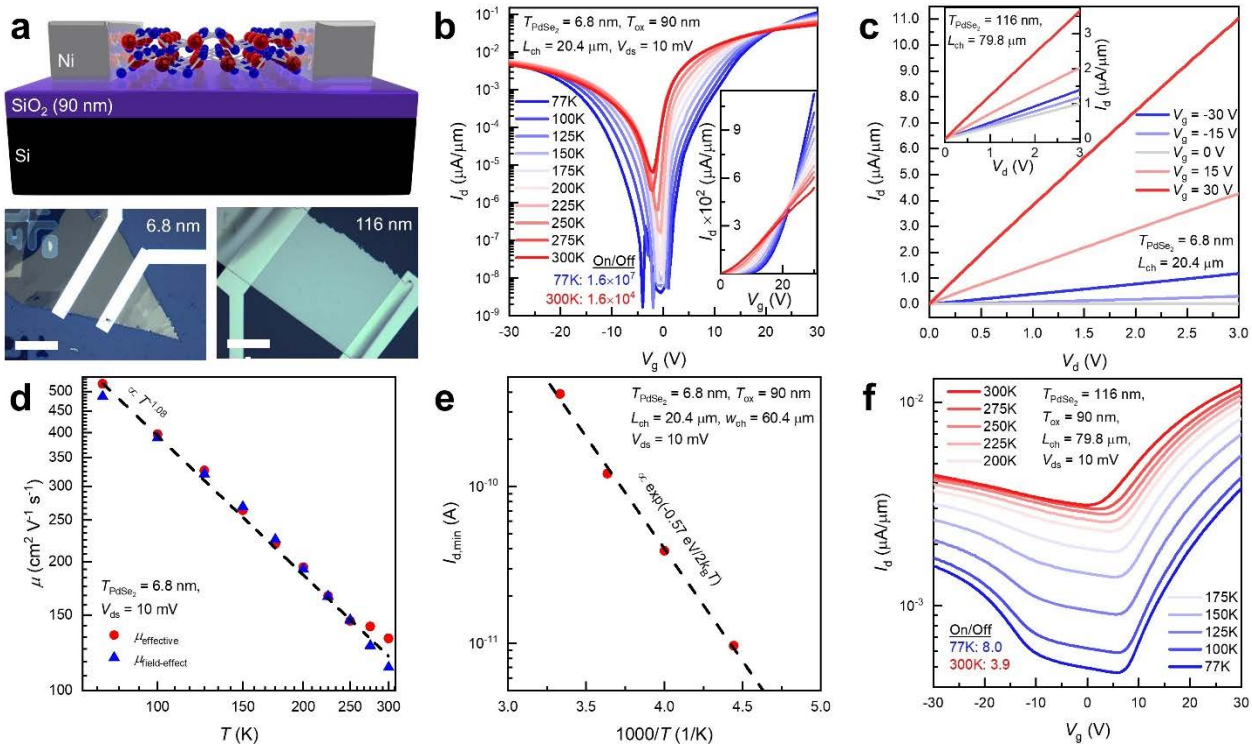

Figure 2.7: Electrical characterization of $PdSe_2$: (a) Back-gated $PdSe_2$ field-effect transistor (FET) structure and optical microscope images of devices with 6.8-nm- and 116-nm-thick $PdSe_2$ flakes. Scale bars are 30 μm. (b) Temperature-dependent I_d-V_g characteristics of the 6.8-nm-thick $PdSe_2$ device measured at a low V_d of 10 mV. The inset shows a plot of the same data in linear-Id scale. (c) I_d-V_d characteristics of the 6.8-nm-thick $PdSe_2$ device inset with those of the 116-nm-thick $PdSe_2$ device. (d) Effective and field-effect mobility of the 6.8-nm-thick $PdSe_2$ device. The dashed line shows a power law fit $\mu_{effective} \propto T^{-\gamma}$ where $\gamma = 1.08$. (e) Arrhenius plot showing the minimum drain-source current ($I_{d,min}$) of the 6.8-nm-thick $PdSe_2$ device as a function of temperature to extract the transport bandgap $E_g = 0.57$ eV. (f) Temperature-dependent I_d-V_g of the 116-nm-thick $PdSe_2$ device measured at $V_d = 10$ mV, showing bulk semiconducting behavior.

Using electron-beam lithography, back-gated $PdSe_2$ field-effect transistors (FETs) were fabricated on 90 nm SiO_2/Si with 100-nm-thick nickel (Ni) contacts. The device structure and optical microscopy images of fabricated devices are shown in Figure 2.7(a). Figure 2.7(b) shows the temperature-dependent I_d-V_g characteristics of the 6.8-nm-thick $PdSe_2$ device measured at a low drain voltage V_d of 10 mV, indicating that the on/off ratio increases as temperature decreases. The inset shows a plot of the same data in linear-I_d scale, clearly showing that the drain-source current $I_{d,max}$ increases with decreasing temperature. We can therefore expect the mobility of this 6.8-nm-thick $PdSe_2$ flake to reach its maximum at low temperatures. The I_d-V_g shows ambipolar conduction since the onset of n-type and p-type conduction is roughly centered around $V_g = 0$ V,

suggesting that the material is roughly intrinsic (i.e. low background doping). The ambipolar characteristics of $PdSe_2$ can be drastically tuned by introducing molecular dopants to $PdSe_2$ while annealed under vacuum [28]. From linear- I_d-V_g plots, we extrapolate room-temperature threshold voltages V_t of 3.65 V and -4.41 V for the 6.8-nm- and 116-nm-thick $PdSe_2$ devices, respectively.

Figure 2.7(c) shows the I_d-V_d characteristics of the 6.8-nm-thick $PdSe_2$ device inset with those of the 116-nm-thick $PdSe_2$ device. Since the drain saturation voltage $V_{d,sat} = V_g - V_t$ exceeds the range of measurement, we do not observe saturation. Additionally, the linear behavior of the I_d-V_d characteristics at low values of V_d suggests minimal contact resistance with small Schottky barrier heights. From these transfer characteristics, we calculated the effective electron mobility, $\mu_{eff} = (dI_d/dV_d)(L_g/w_c)[C_{ox}(V_g - V_t - 0.5V_d)]^{-1}$ and field-effect electron mobility $\mu_{fe} = (dI_d/dV_g)(L_g/w_c)(C_{ox}V_d)^{-1}$ of the 6.8-nm-thick $PdSe_2$ device versus temperature, as shown in Figure 2.7(d). The electron mobility of the 6.8-nm-thick PdSe2 device increases with decreasing temperature. The 6.8-nm-thick PdSe2 device exhibits effective electron mobilities of 130 and 520 cm2 V-1 s-1 at 300 K and 77 K, respectively. We can fit the temperature-dependent mobility of this device with a power law, $\mu_{eff} \propto T^{-\gamma}$ where $\gamma = 1.08$, suggesting that the mobility is limited by phonon scattering [36], [37]. Finally, we extracted a lower bound on the bandgap of a 6.8-nm-thick PdSe2 flake from an Arrhenius plot of the minimum drain-source current Id,min versus the inverse of temperature T by using:

$$I_{d,min} \propto \exp(-E_g / 2kT) \tag{4}$$

where E_g is the transport bandgap and k is the Boltzmann constant (Figure 2.7(e)). We extract a bandgap of 0.57 eV for a 6.8-nm-thick $PdSe_2$ flake. Due to the contribution from trap states, this method is expected to underestimate the bandgap [13]. Finally, to further confirm the optical measurements shown in Figure 2.2(f), we performed temperature-dependent measurements on a $PdSe_2$ transistor fabricated using a bulk (116-nm-thick) crystal, as shown in Figure 2.7(f). Since the thickness of this device is significantly greater than the Debye screening length, the device cannot be fully turned off. Nevertheless, we still observe moderate gate-dependent transport due to the low background doping in $PdSe_2$. This indicates that bulk $PdSe_2$ is semiconducting and is consistent with the absorption measurements shown above.

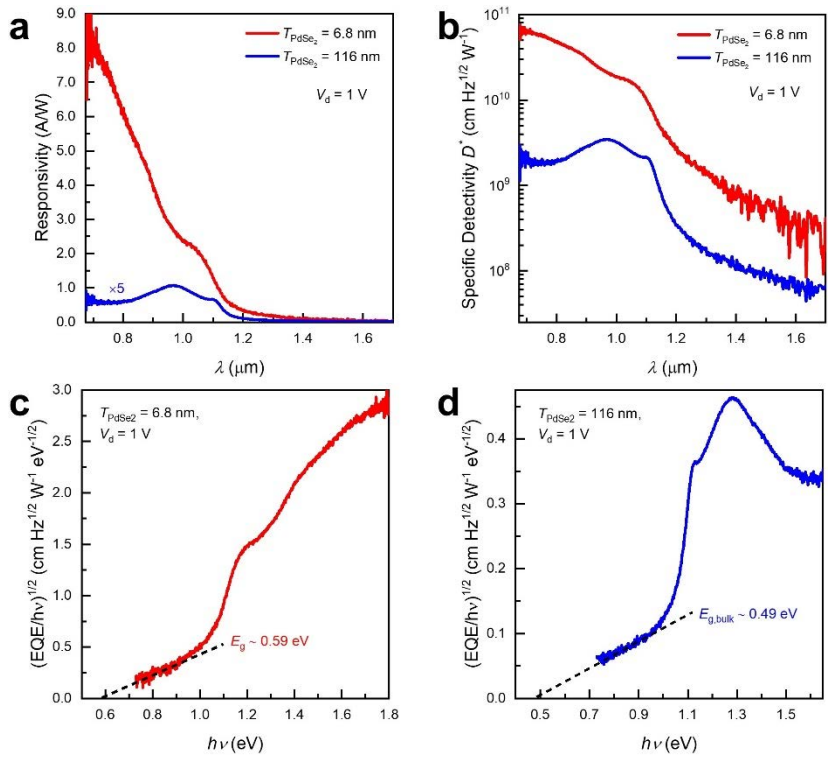

Figure 2.8: Photoresponse of $PdSe_2$ photoconductors: (a) Room-temperature spectral responsivities and (b) specific detectivities D^* of the 6.8-nm- and 116-nm-thick $PdSe_2$ devices shown in Figure 3(a) measured at a drain voltage V_d of 1 V with zero gate voltage V_g applied. (c), (d) Indirect bandgap extraction of a 6.8-nm-thick and a 116-nm-thick $PdSe_2$ flake.

We next investigate the performance of $PdSe_2$ as a photoconductor utilizing the devices discussed in Figure 2.7. Figure 2.8(a) shows the room-temperature spectral responsivities of the 6.8-nm- and 116-nm-thick $PdSe_2$ devices shown in Figure 2.7(a). We measured the spectral responsivity of these devices using an FTIR by replacing the internal detector with the $PdSe_2$ devices and focusing its light source on the devices with a CaF_2 lens. The internal deuterated triglycine sulfate (DTGS) in the FTIR was used to find the relative intensity of the light source and a NIST-traceable Ge photodiode to calibrate the illumination intensity of the light source [11]. The responsivity is calculated as $R(\lambda) = I_{ph}(\lambda)/P_{in}(\lambda)$, where I_{ph} is the photocurrent, and Pin is the incident power on the device. The specific detectivity (D^*) is then calculated using:

$$D^* = \frac{\sqrt{A\Delta f}}{\text{NEP}} = \frac{R\sqrt{A\Delta f}}{i_n} \tag{5}$$

where A is the device area, Δf is the integration time, NEP is the noise equivalent power, and $i_n^2 = 2qI_d\Delta f$ is the squared noise current, where I_d is the dark current. Figure 2.8(b) shows the room-temperature spectral D^* of the 6.8-nm- and 116-nm-thick $PdSe_2$ devices. We find a room-temperature D^* of 6.4×10^{10} cm $Hz^{1/2}$ W^{-1} at a wavelength of 0.7 μm for the 6.8-nm-thick $PdSe_2$ device. From a plot of $(EQE/h\nu)^{1/2}$ versus $h\nu$, we extracted 0.59 eV and 0.49 eV as the optical bandgaps for a 6.8-nm- and 116-nm-thick $PdSe_2$ flake, respectively (Figures 2.8(c)–2.8(d)). It is important to note that the photoresponse measurements shown were taken at $V_g = 0$. This was found to give the highest photoresponse and is consistent with the I_d-V_g characteristics which show the lowest dark current for V_g near zero.

2.2 2D Te Characterization

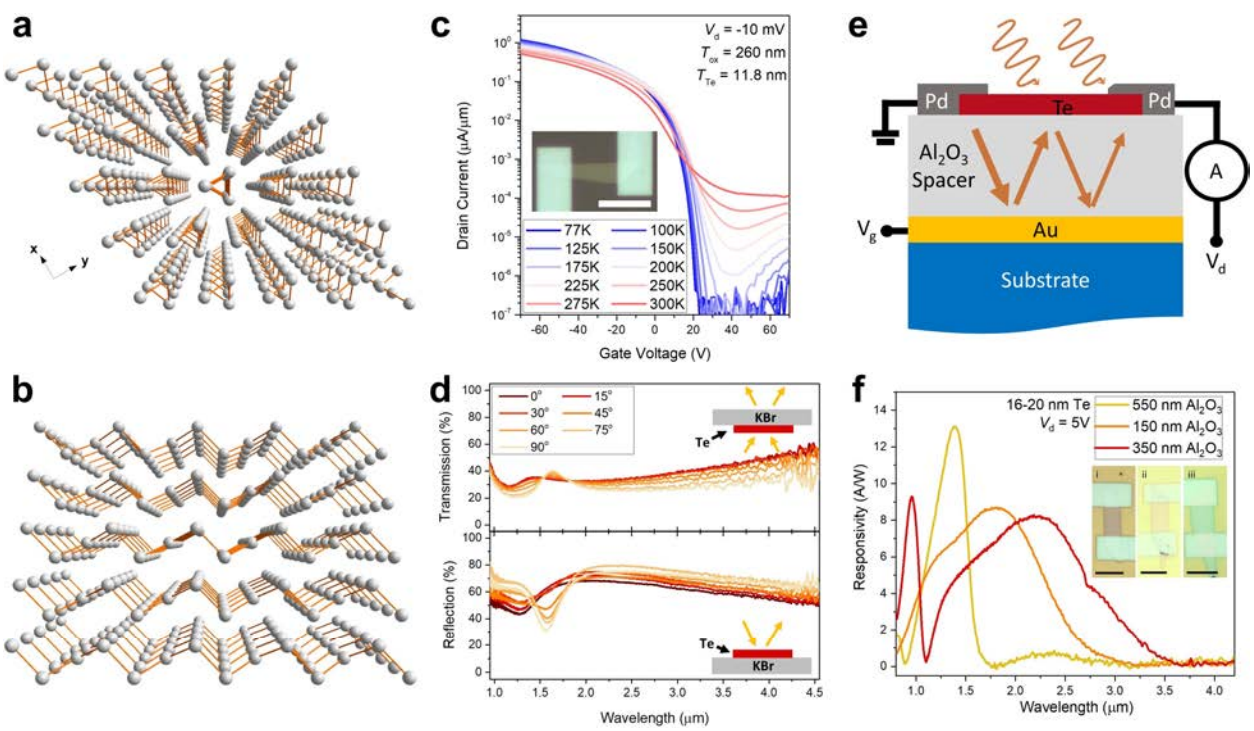

Figure 2.9: 2D Te characterization: Crystal structure of layered Te viewed from the (a) z-axis and the (b) x-axis. (c) Temperature-dependent I_d-V_g characteristics of a 12-nm-thick Te device measured at a low V_d of 10 mV. (d) Polarization-dependent transmission and reflection spectra of

a 111-nm-thick Te flake on a KBr substrate. (e) Optical cavity engineering scheme. (f) Measured responsivities of Te photoconductors fabricated on optical cavities with different Al_2O_3 thicknesses.

Figure 2.9(a)–2.9(b) show the unique crystal structure of 2D Te. Viewed along the x-axis, 2D Te appears layered, however, when viewed along the z-axis, it exhibits a single-molecular chain structure. This gives rise to 2D Te's anisotropic behavior. Figure 2.9(c) shows the temperature-dependent I_d-V_g of a 12-nm-thick Te device measured at V_d = 10 mV. As expected, the on/off ratio increases dramatically with decreasing temperature, approaching ~10^7 at 77K. Figure 2.9(d) shows the anisotropic polarization-resolved transmittance and reflectance of a bulk 111-nm-thick Te flake. To enhance the optical absorption of Te flakes, an optical cavity device structure was used (Figure 2.9(e)). Figure 2.9(f) shows the responsivities of Te photoconductors using optical cavities of varying Al_2O_3 thicknesses. The peak responsivity may be tuned using optical cavity engineering, allowing a Te photoconductor to fully capture the SWIR band.

2.3 2D $PtS_{2-x}Se_x$ Characterization

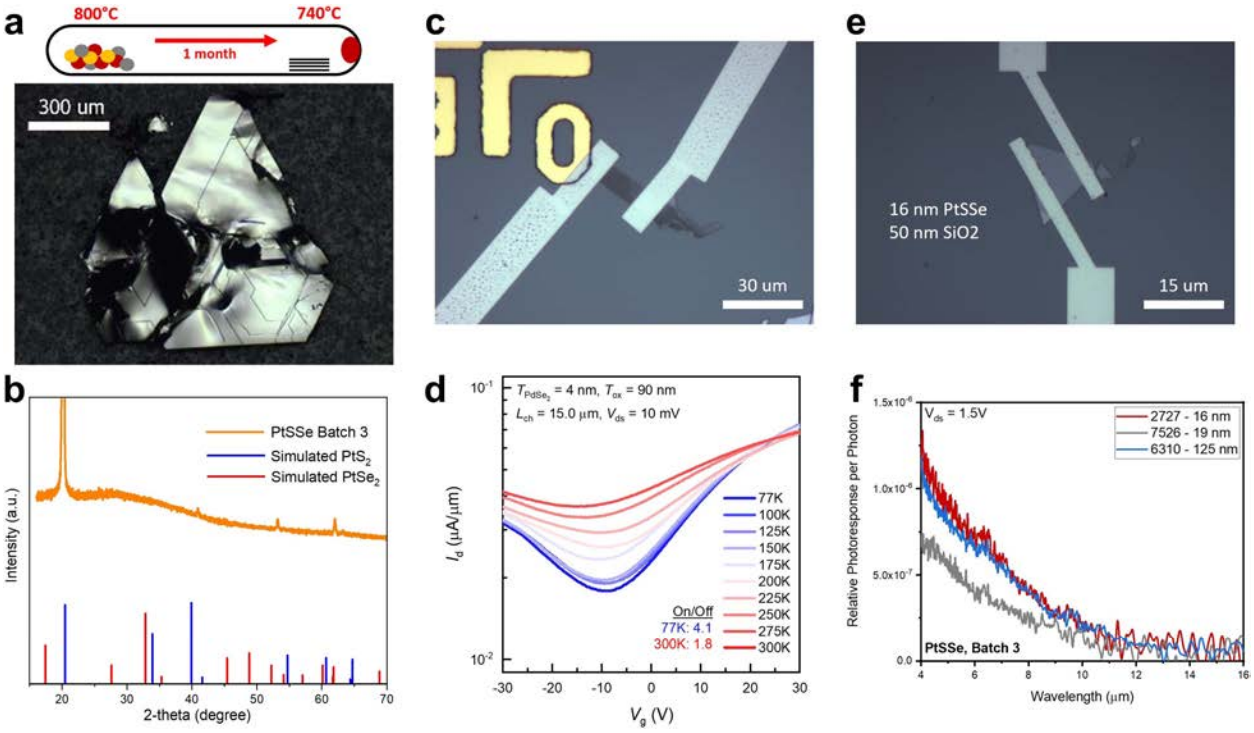

Figure 2.10: 2D $PtS_{2-x}Se_x$ characterization: (a) chemical vapor transport (CVT) growth scheme and optical microscope image of an as-grown $PtS_{2-x}Se_x$ bulk single crystal. (b) Measured XRD spectrum of a bulk $PtS_{2-x}Se_x$ crystal and simulated XRD spectra of pure PtS_2 and $PtSe_2$. (c) Optical microscope image of a 4-nm-thick $PtS_{2-x}Se_x$ device. (d) Temperature-dependent I_d-V_g characteristics of the 4-nm-thick $PtS_{2-x}Se_x$ device measured at a low V_d of 10 mV. (e) Optical microscope image of a 16-nm-thick $PtS_{2-x}Se_x$ device. (f) Measured photoresponse of a 16-, 19-, and 125-nm-thick $PtS_{2-x}Se_x$ device, showing LWIR response up to 11 μm.

$PtS_{2-x}Se_x$ was grown by chemical vapor transport (CVT). Figure 2.10(a) shows a schematic of the CVT process, which involves loading Pt:S:P:Se powders in the atomic ratio 1:1:1:3 in a sealed ampoule under vacuum, loading the ampoule in a furnace with a temperature gradient (800 °C on the side of the ampoule with the powders and 740 °C on the single crystal deposition side), and waiting for a month. Figure 2.10(a) also shows an optical microscope image of an as-grown bulk $PtS_{2-x}Se_x$ single crystal. The XRD spectrum of this crystal is shown in Figure 2.10(b) along with simulated spectra of pure PtS_2 and $PtSe_2$. The rightmost XRD peaks of the crystal appear to be in between those of pure PtS_2 and $PtSe_2$. This is promising, as varying the Se concentration x in $PtS_{2-x}Se_x$ should yield intermediate alloys between pure PtS_2 and $PtSe_2$. Thin layers of $PtS_{2-x}Se_x$ were mechanically exfoliated from this bulk single crystal. Figure 2.10(c) shows a fabricated 4-nm-thick $PtS_{2-x}Se_x$ device. Its temperature-dependent I_d-V_g is shown in Figure 2.10(d). Since $PtS_{2-x}Se_x$ is near metallic, the on/off ratios are incredibly low (1.8 and 4.1 at 300K and 77K, respectively). Figure 2.10(e) shows a fabricated 16-nm-thick $PtS_{2-x}Se_x$ device. Its photoresponse along with those of thicker flakes is shown in Figure 2.10(f), showing LWIR absorption up to 11 μm. The Se concentration for these devices is just 71%. Pushing the Se concentration even higher will likely result in LWIR absorption beyond 11 μm.

Chapter 3

Conclusion

3.1 2D $PdSe_2$

We have performed a systematic study on the optical and electrical properties of $PdSe_2$, a layered two-dimensional pentagonal semiconductor with an indirect bandgap ranging from ~0.5–1.37 eV. We found that a 6.8-nm-thick $PdSe_2$ flake-based transistor has effective electron mobilities of 130 and 520 $cm^2 V^{-1} s^{-1}$ at 300K and 77K, respectively. The same transistor can serve as a SWIR photoconductive detector with a peak D^* of 6.4×10^{10} cm $Hz^{1/2} W^{-1}$ at 0.7 μm with a band edge at 1.94 μm. Given the promising preliminary values of D^* for our simple device structure, further optimization, e.g. optical cavity substrate engineering, may allow the use of $PdSe_2$ for high-performance SWIR photodetectors [13]. Most importantly, through different measurements, we have determined that $PdSe_2$ does not undergo a semiconductor to metal transition with increasing thickness. This finding changes the outlook for the potential application space in which $PdSe_2$ may be used without further manipulating the material's band structure, e.g. by strain [38], [39] or defect [14] engineering.

3.2 2D Te

We have characterized solution-synthesized 2D Te in terms of electrical transport and anisotropic optical absorption and photoresponse. Optical cavity engineering was used to tune the peak responsivity of Te photoconductors, allowing for full SWIR band coverage. This optical cavity engineering technique may be applied to any 2D material to shift its peak responsivity within the material's bandgap range. This can be very useful when optimizing a photodetector to perform in a specific wavelength range.

3.3 2D $PtS_{2-x}Se_x$

To our knowledge, we have developed the second LWIR 2D material, $PtS_{2-x}Se_x$, which outperforms $PtSe_2$ in terms of responsivity and scalability. In our experience, exfoliating thin layers of $PtS_{2-x}Se_x$ is by far more likely than exfoliating thin layers of pure $PtSe_2$, which is likely due to the greater S concentration (pure PtS_2 yields even more thin flakes). The CVT method used to grow $PtS_{2-x}Se_x$ is easily reproducible, and we have shown that alloying can be effective in designing materials with desirable "intermediate" traits.

Bibliography

[1] H. P. Boehm, A. Clauss, G. O.Fischer, and U. Hofmann, “Das Adsorptionsverhalten sehr dünner Kohlenstoff-Folien.” Z. Anorg. Allg. Chem. 316, 119 (1962).

[2] R. F. Frindt and A. D. Yoffe, “Physical properties of layer structures: optical properties and photoconductivity of thin crystals of molybdenum disulphide,” Proc. R. Soc. Lond. A 273, 69−83 (1963).

[3] R. F. Frindt, “Single Crystals of MoS2 Several Molecular Layers Thick,” J. Appl. Phys. 37, 1928−1929 (1966).

[4] K. S. Novoselov, A. K. Geim, S. V. Morozov, D. Jiang, Y. Zhang, S. V. Dubonos, I. V. Grigorieva, A. and A. Firsov, “Electric Field Effect in Atomically Thin Carbon Films,” Science 306, 666−669 (2004).

[5] C. Berger, Z. Song, T. Li, X. Li, A. Y. Ogbazghi, R. Feng, Z. Dai, A. N. Marchenkov, E. H. Conrad, P. N. First, and W. A. de Heer, “Ultrathin Epitaxial Graphite: 2D Electron Gas Properties and a Route toward Graphene-based Nanoelectronics,” J. Phys. Chem. B 108, 19912−19916 (2004).

[6] M. Amani, D.-H. Lien, D. Kiriya, J. Xiao, A. Azcatl; J. Noh, S. R. Madhvapathy, R. Addou, S. Kc, M. Dubey, K. Cho, R. M. Wallace, S.-C. Lee, J.-H. He, J. W. Ager, X. Zhang, E. Yablonovitch, and A. Javey, “Near-Unity Photoluminescence Quantum Yield in MoS2,” Science 350, 1065−1068 (2015).

[7] M. Amani, P. Taheri, R. Addou, G. H. Ahn, D. Kiriya, D.-H. Lien, J. W. Ager, R. M. Wallace, and A. Javey, “Recombination Kinetics and Effects of Superacid Treatment in Sulfur- and Selenium Based Transition Metal Dichalcogenides,” Nano Lett. 16, 2786−2791 (2016).

[8] S. B. Desai, S. R. Madhvapathy, A. B. Sachid, J. P. Llinas, Q. Wang, G. H. Ahn, G. Pitner, M. J. Kim, J. Bokor, C. Hu, H.-S. P. Wong, and A. Javey, “MoS2 Transistors with 1-Nanometer Gate Lengths,” Science 354, 99−102 (2016).

[9] H. Fang, S. Chuang, T. C. Chang, K. Takei, T. Takahashi, and A. Javey, “High-Performance Single Layered WSe2 p-FETs with Chemically Doped Contacts,” Nano Lett. 12, 3788−3792 (2012).

[10] R. B. Barnes, “Thermography of the Human Body: Infrared-Radiant Energy Provides New Concepts and Instrumentation for Medical Diagnosis,” Science 140, 870–877 (1963).

[11] M. Amani, E. Regan, J. Bullock, G. H. Ahn, and A. Javey, “Mid-Wave Infrared Photoconductors Based on Black Phosphorus-Arsenic Alloys,” ACS Nano 11, 11724–11731 (2017).

[12] J. Bullock, M. Amani, J. Cho, Y-Z. Chen, G. H. Ahn, V. Adinolfi, V. R. Shrestha, Y. Gao, K. B. Crozier, Y.-L. Chueh, and A. Javey, “Polarization-resolved black phosphorus/molybdenum disulfide mid-wave infrared photodiodes with high detectivity at room temperature,” Nat. Photonics 12, 601−607 (2018).

[13] M. Amani, C. Tan, G. Zhang, C. Zhao, J. Bullock, X. Song, H. Kim, V. R. Shrestha, Y. Gao, K. B. Crozier, M. Scott, and A. Javey, “Solution-Synthesized High-Mobility Tellurium Nanoflakes for Short-Wave Infrared Photodetectors,” ACS Nano 12, 7253–7263 (2018).

[14] X. Yu, P. Yu, D. Wu, B. Singh, Q. Zeng, H. Lin, W. Zhou, J. Lin, K. Suenaga, Z. Liu, and Q. J. Wang, “Atomically Thin Noble Metal Dichalcogenide: A Broadband Mid-Infrared Semiconductor,” Nat. Commun. 9, 1545 (2018).

[15] A. D. Oyedele, S. Yang, L. Liang, A. A. Puretzky, K. Wang, J. Zhang, P. Yu, P. R. Pudasaini, A. W. Ghosh, Z. Liu, C. M. Rouleau, B. G. Sumpter, M. F. Chisholm, W. Zhou, P. D. Rack, D. B. Geohegan, and K. Xiao, “PdSe2: Pentagonal Two-Dimensional Layers with High Air Stability for Electronics,” J. Am. Chem. Soc. 139, 14090–14097 (2017).

[16] M. Long, Y. Wang, P. Wang, X. Zhou, H. Xia, C. Luo, S. Huang, G. Zhang, H. Yan, Z. Fan, X. Wu, X. Chen, W. Lu, and W. Hu, “Palladium Diselenide Long-Wavelength Infrared Photodetector with High Sensitivity and Stability,” ACS Nano 13, 2511–2519 (2019).

[17] G. Zhang, M. Amani, A. Chaturvedi, C. Tan, J. Bullock, X. Song, H. Kim, D.-H. Lien, M. C. Scott, H. Zhang, and A. Javey, "Optical and Electrical Properties of Two-Dimensional Palladium Diselenide,” under review by Appl. Phys. Lett. (2019).

[18] C. L. Tan, X. H. Cao, X.-J. Wu, Q. Y. He, J. Yang, X. Zhang, J. Z. Chen, W. Zhao, S. K. Han, G.-H. Nam, M. Sindoro, and H. Zhang, "Recent Advances in Ultrathin Two-Dimensional Nanomaterials," Chem. Rev. 117, 6225–6331 (2017).

[19] 2P. Miró, M. Ghorbani-Asl, and T. Heine, "Two Dimensional Materials Beyond MoS2: Noble-Transition-Metal Dichalcogenides," Angewandte Chemie 53, 3015–3018 (2014).

[20] A. Ciarrocchi, A. Avsar, D. Ovchinnikov, and A. Kis, "Thickness-Modulated Metal-to-Semiconductor Transformation in a Transition Metal Dichalcogenide," Nat. Commun. 9, 919 (2018).

[21] Y. Zhao, J. Qiao, Z. Yu, P. Yu, K. Xu, S. P. Lau, W. Zhou, Z. Liu, X. Wang, W. Ji, and Y. Chai, "High-Electron-Mobility and Air-Stable 2D Layered PtSe2 FETs," Adv. Mater. 29, 1604230 (2017).

[22] M. Ghorbani-Asl, A. Kuc, P. Miró, and T. Heine, "A Single-Material Logical Junction Based on 2D Crystal PdS2," Adv. Mater. 28, 853−856 (2016).

[23] Y. Zhao, J. Qiao, P. Yu, Z. Hu, Z. Lin, S. P. Lau, Z. Liu, W. Ji, and Y. Chai, "Extraordinarily Strong Interlayer Interaction in 2D Layered PtS2," Adv. Mater. 28, 2399–2407 (2016).

[24] M. Yan, H. Huang, K. Zhang, E. Wang, W. Yao, K. Deng, G. Wan, H. Zhang, M. Arita, H. Yang, Z. Sun, H. Yao, Y. Wu, S. Fan, W. Duan, and S. Zhou, "Lorentz-Violating Type-II Dirac Fermions in Transition Metal Dichalcogenide PtTe2," Nat. Commun. 8, 257 (2017).

[25] M. Yan, H. Huang, K. Zhang, E. Wang, W. Yao, K. Deng, G. Wan, H. Zhang, M. Arita, H. Yang, Z. Sun, H. Yao, Y. Wu, S. Fan, W. Duan, and S. Zhou, "Lorentz-Violating Type-II Dirac Fermions in Transition Metal Dichalcogenide PtTe2," Nat. Commun. 8, 257 (2017).

[26] O. J. Clark, M. J. Neat, K. Okawa, L. Bawden, I. Marković, F. Mazzola, J. Feng, V. Sunko, J. M. Riley, W. Meevasana, J. Fujii, I. Vobornik, T. K. Kim, M. Hoesch, T. Sasagawa, P. Wahl, M. S. Bahramy, and P. D. C. King, "Fermiology and Superconductivity of Topological Surface States in PdTe2," Phys. Rev. Lett. 120, 156401 (2018).

[27] S. Das, Amit, A. Sirohi, L. Yadav, S. Gayen, Y. Singh, and G. Sheet, "Conventional superconductivity in the type-II Dirac semimetal PdTe2," Phys. Rev. B 97, 014523 (2018).

[28] W. L. Chow, P. Yu, F. Liu, J. Hong, X. Wang, Q. Zeng, C.-H. Hsu, C. Zhu, J. Zhou, X. Wang, J. Xia, J. Yuan, Y. Chen, D. Wu, T. Yu, Z. Shen, H. Lin, C. Jin, B. K. Tay, and Z. Liu, "High Mobility 2D Palladium Diselenide Field-Effect Transistors with Tunable Ambipolar Characteristics," Adv. Mater. 29, 1602969 (2017).

[29] Y. Wang, G. Qiu, R. Wang, S. Huang, Q. Wang, Y. Liu, Y. Du, W. A. Goddard, Kim, M. J.; Xu, X.; Ye, P. D.; Wu, W., "Field-Effect Transistors made from Solution-Grown Two-Dimensional Tellurene," Nat. Electron. 1, 228−236 (2018).

[30] S. Zhang, J. Zhou, Q. Wang, X. Chen, Y. Kawazoe, and P. Jena, "Penta-Graphene: A New Carbon Allotrope," Proc. Nat. Acad. Sci. 112, 2372–2377 (2015).

[31] S. Liu, B. Liu, X. Shi, J. Lv, S. Niu, M. Yao, Q. Li, R. Liu, T. Cui, and B. Liu, "Two-Dimensional Penta-BP5 Sheets: High-Stability, Strain-Tunable Electronic Structure and Excellent Mechanical Properties," Sci. Rep. 7, 2404 (2017).

[32] S. B. Desai, S. R. Madhvapathy, M. Amani, D. Kiriya, M. Hettick, M. Tosun, Y. Zhou, M. Dubey, J. W. Ager III, D. Chrzan, and A. Javey, "Gold-Mediated Exfoliation of Ultralarge Optoelectronically-Perfect Monolayers," Adv. Mater. 28, 4053–4058 (2016).

[33] O. S. Heavens, Optical Properties of Thin Solid Films (Dover, New York, 1991) p. 55–59.

[34] P. Liu, P. Longo, A. Zaslavsky, and D. Pacifici, "Optical Bandgap of Single- and Multi-Layered Amorphous Germanium Ultra-Thin Films," J. Appl. Phys. 119, 014304 (2016).

[35] H. Zhang, Y. Ma, Y. Wan, X. Rong, Z. Xie, W. Wang, and L. Dai, "Measuring the Refractive Index of Highly Crystalline Monolayer MoS2 with High Confidence," Sci. Rep. 5, 8440 (2015).

[36] B. Radisavljevic, and A. Kis, "Mobility Engineering and a Metal Insulator Transition in Monolayer MoS2," Nat. Mater. 12, 815−820 (2013).

[37] S. Xu, Z. Wu, H. Lu, Y. Han, G. Long, X. Chen, T. Han, W. Ye, Y. Wu, J. Lin, J. Shen, Y. Cai, Y. He, F. Zhang, R. Lortz, C. Cheng, and N. Wang, "Universal Low-Temperature Ohmic Contacts for Quantum Transport in Transition Metal Dichalcogenides," 2D Mater. 3 021007 (2016).

[38] X. Liu, H. Zhou, B. Yang, Y. Qu, and M. Zhao, “Strain-Modulated Electronic Structure and Infrared Light Adsorption in Palladium Diselenide Monolayer,” Sci. Rep. 7, 39995 (2017).

[39] S. B. Desai, G. Seol, J. S. Kang, H. Fang, C. Battaglia, R. Kapadia, J. W. Ager, J. Guo, and A. Javey, “Strain-Induced Indirect to Direct Bandgap Transition in Multilayer WSe2,” Nano Lett. 14, 4592−4597 (2014).